

Mapping propagation of collective modes in Bi_2Se_3 and $\text{Bi}_2\text{Te}_{2.2}\text{Se}_{0.8}$ topological insulators by near-field terahertz nanoscopy

Eva Arianna Aurelia Pogna^{1✉}, Leonardo Viti¹, Antonio Politano ², Massimo Brambilla³, Gaetano Scamarcio³ & Miriam Serena Vitiello ^{1✉}

Near-field microscopy discloses a peculiar potential to explore novel quantum state of matter at the nanoscale, providing an intriguing playground to investigate, locally, carrier dynamics or propagation of photoexcited modes as plasmons, phonons, plasmon-polaritons or phonon-polaritons. Here, we exploit a combination of hyperspectral time domain spectroscopy nano-imaging and detectorless scattering near-field optical microscopy, at multiple terahertz frequencies, to explore the rich physics of layered topological insulators as Bi_2Se_3 and $\text{Bi}_2\text{Te}_{2.2}\text{Se}_{0.8}$, hyperbolic materials with topologically protected surface states. By mapping the near-field scattering signal from a set of thin flakes of Bi_2Se_3 and $\text{Bi}_2\text{Te}_{2.2}\text{Se}_{0.8}$ of various thicknesses, we shed light on the nature of the collective modes dominating their optical response in the 2-3 THz range. We capture snapshots of the activation of transverse and longitudinal optical phonons and reveal the propagation of sub-diffractive hyperbolic phonon-polariton modes influenced by the Dirac plasmons arising from the topological surface states and of bulk plasmons, prospecting new research directions in plasmonics, tailored nanophotonics, spintronics and quantum technologies.

¹NEST, CNR-Istituto Nanoscienze and Scuola Normale Superiore, Piazza San Silvestro 12, 56127 Pisa, Italy. ²Department of Physical and Chemical Sciences, University of L'Aquila, via Vetoio 1, 67100 L'Aquila, Italy. ³Dipartimento Interateneo di Fisica, Università degli Studi e Politecnico di Bari, and CNR-Istituto di Fotonica e Nanotecnologie, via Amendola 173, 70126 Bari, Italy. ✉email: evaariannaurelia.pogna@cnr.it; miriam.vitiello@sns.it

Rhombohedral layered compounds of bismuth with group VI elements as Bi_2Se_3 , Bi_2Te_3 and their alloys have attracted renewed interest as prime candidates for the development of photonic devices exploiting their topological nature,^{1,2} thanks to their thickness-dependent bandgap and to the electronic dispersion of their topological surface states (TSS)³. These topological insulators (TIs)¹ are semiconductors in the bulk, exhibiting metallic conduction at the surface, activated by the TSS, which form a Dirac cone around the Γ point of a hexagonal Brillouin zone².

TIs provide a versatile platform for investigating quantum phenomena and for applications in electronics and photonics: with almost the same high-absorbance of graphene⁴, they can exploit a tunable surface bandgap⁵; their optical and electronic properties can be engineered by changing the material stoichiometry⁶, and the two-dimensional electron gas (2DEG) arising from the TSS can support collective excitation (Dirac plasmon) at terahertz (THz) frequencies^{7,8}. This opens intriguing perspectives for a variety of application fields, such as quantum computing⁹, spintronics¹⁰, and photodetection⁶.

Some of these applications may benefit from the exploitation of electronic collective excitations, like plasmons,^{11,12} plasmon-polaritons¹³—hybrid light–matter modes involving the collective oscillations of charge carriers, phonons¹⁴ or phonon-polaritons^{15,16}, whose wavelength can be electrically controlled. However, capturing these modes on the TSS of a TI or even in the bulk is a very demanding task: it requires sophisticated optical techniques capable of imaging at their exact frequency or mapping their long-range propagation; very importantly, the correct identification of TSS requires the knowledge of their complete energy/momentum dispersion, that can be only unveiled in TI samples showing sufficiently high structural quality (both stoichiometric and crystallographic)^{17,18}.

Amplitude- and phase-resolved scattering near-field optical microscopy (s-SNOM)^{14,15,19–25} can allow access to the spatial variation of complex-valued dielectric response of layered 2D materials, heterostructures and low dimensional systems, therefore providing the sub-diffractive spatial resolution required to investigate light–matter interaction at the nanoscale. Moreover, s-SNOM is the ideal tool to investigate polaritons since its sharp tip acts both as a launcher and as a detector of propagating collective modes¹⁵. A large variety of interferometric approaches has been developed in the last years, allowing amplitude and phase-resolved s-SNOM imaging in the visible and infrared spectral ranges^{19,20}, including fs pulsed laser sources and electro-optic sampling detection in the THz range,²¹ microwave circuitry in the sub-THz range^{22,23} or interferometric techniques^{24,25} strongly limited by the poor dynamic range of the cryogenically cooled bolometric detectors needed to measure the typically small s-SNOM THz signals.

At THz frequencies, the dielectric response of TIs based on bismuth chalcogenides is characterized by longitudinal (LO) and transverse (TO) optical phonons that identify frequency regions of hyperbolicity, within which the dielectric permittivities along the in-plane and out-of-plane directions have an opposite sign and the isofrequency surfaces of the extraordinary rays are hyperboloids in the momentum space^{26,27}. Hyperbolic phonon-polariton modes have been intensively investigated in hexagonal boron nitride (hBN)^{15,28,29}, where they occur at mid-infrared frequencies, due to their unique capability to support the propagation of light with momentum far exceeding the free-space value without evanescent decay^{15,28}. Remarkably, in TIs, these polaritons, that have great potential for THz waveguiding, can interact with the electrons associated to the TSS resulting in doping tunable dispersion³⁰.

In this letter, we exploit an innovative combination of hyperspectral time-domain spectroscopy (TDS) nano-imaging³¹ and detectorless scattering near-field optical microscopy (s-SNOM)¹⁴, at three distinctive pumping energies in the far-infrared, to explore the rich physics of thin flakes of Bi_2Se_3 and $\text{Bi}_2\text{Te}_{2.2}\text{Se}_{0.8}$, having different

thicknesses. We select Bi_2Se_3 because of its simple electronic structure, showing a topologically nontrivial direct energy gap of 0.3 eV^{32,33}, about ten times higher than thermal excitation at RT³⁴ and higher than that of Bi_2Te_3 , having an energy gap of about 0.15 eV³⁵. We then investigate $\text{Bi}_2\text{Te}_{(3-3x)}\text{Se}_{3x}$ because, on one side, the energy gap is expected to increase rapidly with x , reaching values >0.2 eV for $3x = 0.8$ ³⁵, and on the other side, the Fermi level of high Te-content alloys, like $\text{Bi}_2\text{Te}_{2.2}\text{Se}_{0.8}$, crosses only the TSS Dirac cone, meaning that its TSS electrons behave as an ideal 2D electron gas³⁶.

Theoretical proposals² on TSS require the chemical potential to lie at, or to approach, the surface Dirac point. However, the surface Fermi level of a TI depends on the detailed electrostatics of the surface and it is not necessarily at the Dirac point. In a naturally grown Bi_2Se_3 , the bulk Fermi energy does not lie in the gap³³. The material displays n-type behavior and usually exhibits significant contributions from the bulk carriers to the total conductivity^{33,34,37–39}. One reason for the shift of the chemical potential into the conduction band is donor doping, typically induced by Se vacancies² and antisite defects⁴⁰. Another effect, which can interfere with the ideal TI response, occurs when the bulk bands cross the Fermi level near the material surface, generating a 2DEG of massive carriers close to the surface if the bands bend downwards⁴¹. This has been observed in similarly grown single-crystal Bi_2Se_3 when exposed to the atmosphere after cleaving⁴², as a consequence of extrinsic defects or molecular adsorption at the surface³⁶. The 2DEG is believed to be confined within 20 nm from the surface in Bi_2Se_3 ³⁶ and coexists with the TSS. Engineering the $\text{Bi}_2\text{Te}_{(3-3x)}\text{Se}_{3x}$ stoichiometry can therefore allow tuning the TI physics, on purpose.

Our combination of two different near-field techniques allows identifying optically activated TO and LO phonons, and reveals massive bulk plasmons, arising from the 2DEG originated from the band bending at the sample surfaces in Bi_2Se_3 , and hybrid plasmon–phonon-polariton modes propagating from the edge of the $\text{Bi}_2\text{Te}_{2.2}\text{Se}_{0.8}$ flakes. Remarkably, this represents the first experimental demonstration of hybrid plasmon–phonon-polariton modes reported to date in topological insulators and paves the way for novel sub-diffractive and tunable THz polaritonic waveguides.

Results and discussion

Samples. Flakes of thickness d in the range 15–200 nm and lateral size in the range 0.2–4 μm are obtained by mechanical exfoliation on a 350- μm -thick silicon wafer, with a 300 nm thin insulating SiO_2 top-layer. The micro Raman characterization of prototypical flakes of Bi_2Se_3 and $\text{Bi}_2\text{Te}_{2.2}\text{Se}_{0.8}$ is reported in Supplementary Fig. 1a, b, respectively. Bi_2Se_3 and Bi_2Te_3 crystallize in tetradymites with rhombohedral crystal structure endowed with D_{3d}^5 space group symmetry and five atoms per unit cell. The structure consists of quintuple layers (QL) stacked via weak van der Waals forces, which permit an easy mechanical exfoliation, orthogonally to the trigonal c -axis. One QL corresponds to a 1.42 nm thick crystal of Bi_2Se_3 and to 1 nm for $\text{Bi}_2\text{Te}_{2.2}\text{Se}_{0.8}$. Within each QL, pictogen (Bi) and chalcogen atoms (Se, Te) are held together by ionic covalent bonds. The different bond strength and character result in a strong in-plane/out-of-plane anisotropy in the thermal, electronic and dielectric properties of these materials.

Time-domain near-field spectroscopy: the role of hyperbolic phonons. Hyperspectral THz nano-imaging³¹ is performed by coupling the s-SNOM microscope to a THz TDS system based on photoconductive (PC) antennas (Menlo TERA15 FC), as schematically depicted in Fig. 1a.

The broadband THz pulse produced by the transmitter antenna, with a spectrum spanning the 4–140 cm^{-1} range, is focused on the atomic force microscope (AFM) tip of the s-SNOM and the forward-scattered field is detected as a function of the time delay from the gate

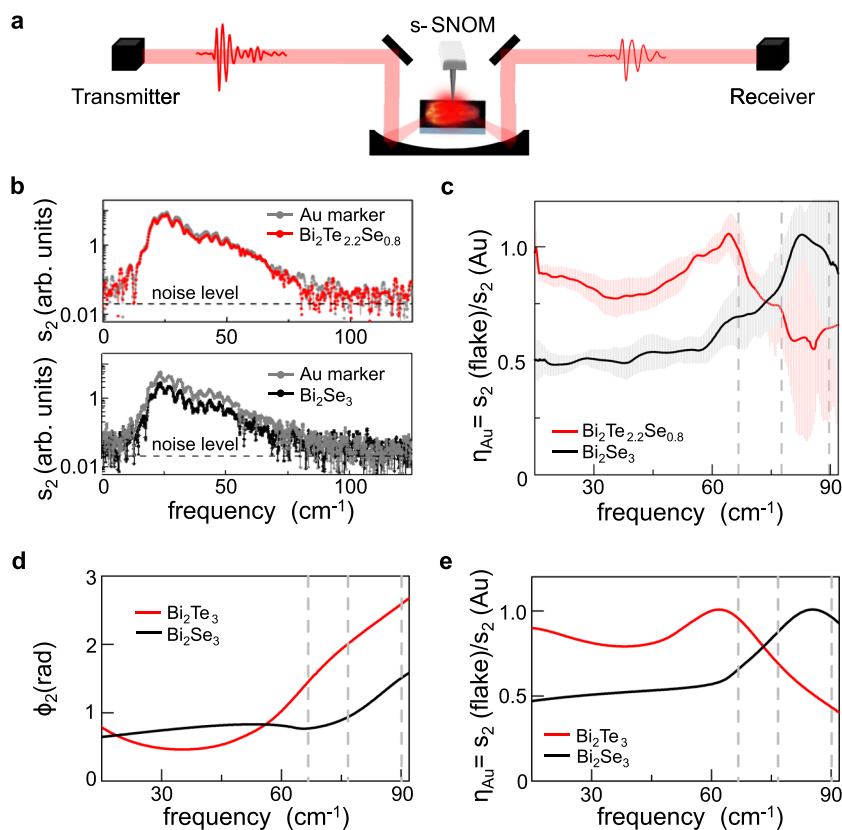


Fig. 1 Hyperspectral THz nano-imaging of TI. **a** Sketch of the hyperspectral THz nano-imaging experiment based on detection of the THz field forward scattered by the AFM tip of the s-SNOM with a TDS system based on two photoconductive antennas: the receiver and the transmitter. **b** Spectra of second-order demodulated signal s_2 scattered by thick flakes of Bi_2Se_3 ($d = 86$ nm, lower panel, black circles and line) and $\text{Bi}_2\text{Te}_{2.2}\text{Se}_{0.8}$ flakes ($d = 76$ nm, upper panel, red circles and line) as compared to the scattered spectra from a 140 nm thick Au reference marker (gray circles and line). **c** Contrast η_{Au} evaluated dividing the average of 60 spectra s_2 scattered by $\text{Bi}_2\text{Te}_{2.2}\text{Se}_{0.8}$ (red line) and Bi_2Se_3 (black line) by the average of 60 spectra measured on Au reference markers placed near the flakes after smoothing each curve with the average on 20 points window. The error bars are evaluated as standard deviation. **d, e** Near-field phase ϕ_2 (**d**) and contrast η_{Au} (**e**) of the second-order demodulated signal s_2 as a function of frequency for bulk Bi_2Se_3 (black line) and Bi_2Te_3 (red line) retrieved via numerical inversion⁵¹ of the finite-dipole model on a four-layer structure (see Supplementary Fig. 6). Gray dashed lines in panels c–e mark the probing frequencies of the detectorless near-field experiment.

pulse by a second PC antenna, the receiver, working in reverse mode. This technique combines broadband spectral coverage with sub-diffractive spatial resolution of ~ 260 nm (see Supplementary Fig. 4) achieved by using an AFM tip with apex radius $r = 40$ nm, 80 μm cantilever length (Rocky Mountain Nanotechnology, 25PtIr300B) working in tapping mode, with an oscillation amplitude $A \sim 200$ nm and a tapping frequency $\Omega \sim 20$ kHz.

The detected THz scattered field $S_n = s_n e^{-i\phi}$, with amplitude s_n and phase ϕ , is demodulated at the tapping frequency n th harmonics $\Omega_n = n\Omega$ with $n = 2-4$ to isolate the near-field contribution from the background due to far-field illumination of the tip shaft and sample¹⁹. Images of the near-field scattered amplitude s_n , at a fixed time delay, for thick flakes ($d > 75$ nm) of Bi_2Se_3 and $\text{Bi}_2\text{Te}_{2.2}\text{Se}_{0.8}$ as a function of the demodulation order n , are reported in Supplementary Fig. 2a, b. To find a good compromise between signal intensity and suppression of the far-field background, we investigate the second harmonic near-field signal. This choice is supported by the analysis of the approach curves (Supplementary Fig. 3) at the different demodulation orders.

Nano-THz spectra at fixed positions on thick ($d > 75$ nm) Bi_2Se_3 and $\text{Bi}_2\text{Te}_{2.2}\text{Se}_{0.8}$ flakes and on a reference point on an Au marker are reported in Fig. 1b. Each spectrum is obtained by averaging 60 different spectra acquired with 100 ps time-scan, lasting 45 s, performed in a nitrogen atmosphere to prevent absorption by

water vapor⁴³. Due to the frequency-dependent scattering efficiency of the tip⁴⁴, a signal-to-noise ratio (SNR) > 1.5 is achieved only in the range $15-90$ cm^{-1} . In this range, the two crystals exhibit distinct contrast η_{Au} , evaluated by the ratio of the second-order demodulated spectra s_2 scattered by the flake with that of the Au reference, as routinely done in nano-FTIR spectroscopy⁴⁵. While both compounds show a broad peak in the probed range, the maximum η_{Au} is reached at ~ 80 cm^{-1} for Bi_2Se_3 and at ~ 60 cm^{-1} for $\text{Bi}_2\text{Te}_{2.2}\text{Se}_{0.8}$. This scattering enhancement can be attributed to infrared-active bulk optical phonons⁴⁶⁻⁴⁸. The peak in the near-field scattering intensity of Bi_2Se_3 occurs within the frequency band $\omega_{\text{to}}^{\perp} < \omega < \omega_{\text{to}}^{\parallel}$ identified by the dominant long-wavelength TO optical phonon modes³⁰: the E_u TO ($\omega_{\text{to}}^{\perp} = 64$ cm^{-1}) and the A_{2u} TO ($\omega_{\text{to}}^{\parallel} = 135$ cm^{-1}) phonons, involving atomic vibrations in the plane orthogonal (\perp) and parallel (\parallel) to the trigonal c -axis, respectively. Within this frequency range, the real parts of the permittivity along the directions orthogonal ϵ^{\perp} and parallel ϵ^{\parallel} to the c -axis have an opposite sign ($\text{Re}\{\epsilon^{\perp}\} < 0$, $\text{Re}\{\epsilon^{\parallel}\} > 0$) and Bi_2Se_3 is expected to behave as a hyperbolic material of type II. We can use the vibrational modes of Bi_2Te_3 to model the $\text{Bi}_2\text{Te}_{2.2}\text{Se}_{0.8}$ flake, due to the low dispersion⁴⁶ of the phonon modes of the $\text{Bi}_2\text{Te}_{(3-3x)}\text{Se}_{3x}$ alloy for $x < 1/3$. The lower frequency of the $\text{Bi}_2\text{Te}_{2.2}\text{Se}_{0.8}$ peak can be traced back into the red-shift of E_u and A_{2u} TO phonons with

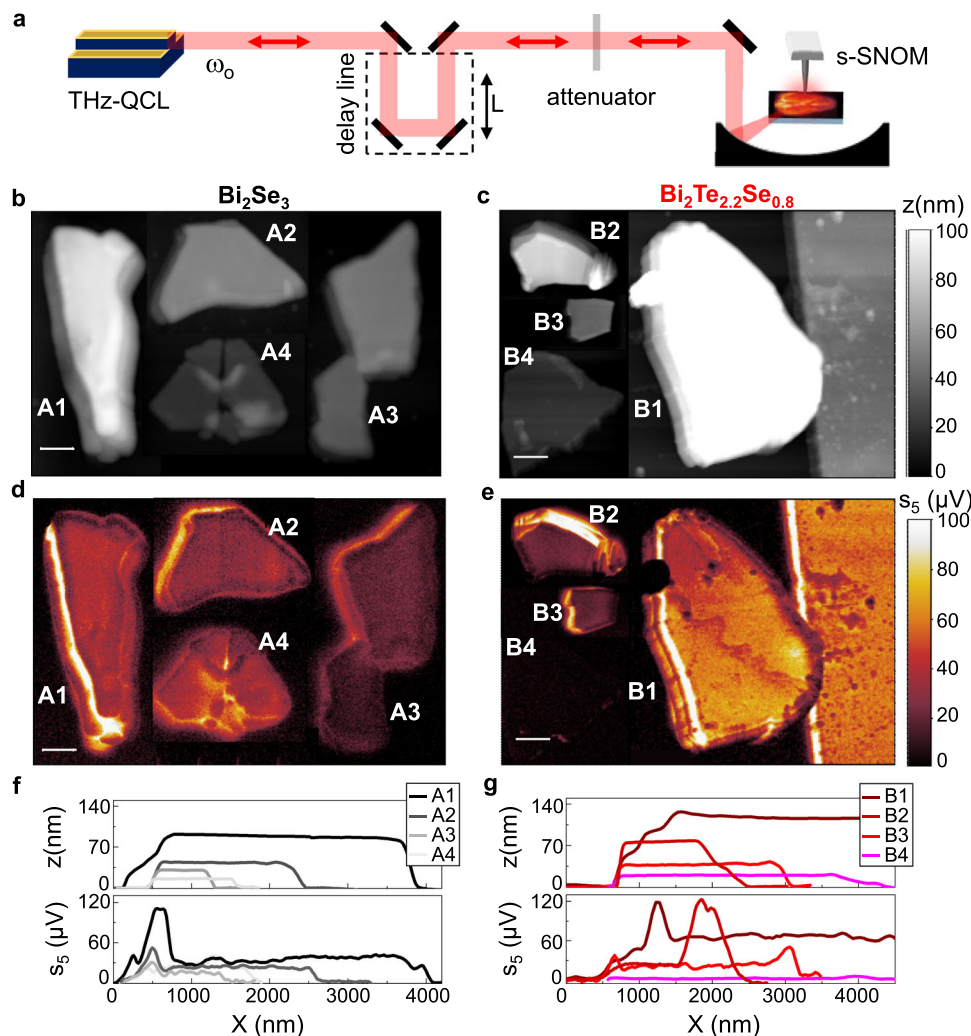


Fig. 2 Self-detection THz nanoscopy of TIs. **a** Sketch of the self-detection nanoscopy experiment based on THz-QCL of frequency $\omega_0 = 66.7, 76.7, 89.7 \text{ cm}^{-1}$ simultaneously serving as source and detector of the backscattered field from the AFM tip of the s-SNOM with a delay-line controlling the length L of the optical path and an attenuator to reduce the feedback intensity. **b, c** Topography maps of four distinctive flakes of Bi_2Se_3 (**a**) and $\text{Bi}_2\text{Te}_{2.2}\text{Se}_{0.8}$ (**b**) of variable thickness z with labels A_i and B_i , respectively, with $i = 1, 2, 3, 4$. **d, e** Near-field maps of the fifth-order self-mixing signal S_5 of the flakes in panels (**b, c**) taken while keeping a fixed external cavity length L , measured with $\omega_0 = 66.7 \text{ cm}^{-1}$ without attenuation. Scale bars in panels (**b–e**) correspond to $1 \mu\text{m}$. **f, g** Line scans of the topography maps z and of the fifth-order self-mixing signal S_5 on four distinctive flakes of Bi_2Se_3 (**f**) and of $\text{Bi}_2\text{Te}_{2.2}\text{Se}_{0.8}$ (**g**), extracted from panels (**b, c**) and (**d, e**) while moving from the substrate to the flakes along a line orthogonal to the flakes edge.

increasing Te-content towards the values reported for Bi_2Te_3 ($\omega_{\text{to}}^{\perp} = 50 \text{ cm}^{-1}$ and $\omega_{\text{to}}^{\parallel} = 95 \text{ cm}^{-1}$)^{46,47}.

Three-dimensional model calculations of the near-field contrast η based on the well-established finite-dipole approximation^{49,50}, considering multiple LO and TO phonon modes, both in \parallel and \perp directions, are reported in the Supplementary Fig. 5a. The model well reproduces the experimental spectra, suggesting that Bi_2Te_3 can reasonably mimic the near-field response of the $\text{Bi}_2\text{Te}_{2.2}\text{Se}_{0.8}$. Moreover, since the exposed surfaces are parallel to the basal plane, the ability of detecting \perp modes implies that the component of the THz near-field orthogonal to the tip-tapping is non-negligible, as previously observed in anisotropic crystals as SiC⁴⁹.

In order to disentangle the dielectric response from the bulk and the surface, we then combine the finite-dipole approach to describe the tip-sample interaction, with a multilayer model for up to four layers and we implement an inversion algorithm to extract the local dielectric function of the surface layer alone⁵¹ (see Supplementary Note 3 and Fig. 6). We note that even if we include a finite bulk carrier density, both Bi_2Se_3 and $\text{Bi}_2\text{Te}_{2.2}\text{Se}_{0.8}$ maintain their hyperbolic behavior as testified by the opposite signs of the real

parts of the bulk dielectric functions in the \parallel and \perp directions (see Supplementary Fig. 6d, e). The comparison between the two models (the multilayer model in Fig. 1e and the bulk model in Supplementary Fig. 5a) clearly unveils that while in Bi_2Se_3 the amplitude contrast is well reproduced by the bulk model and the TSS do not appear to contribute to the near-field response (black traces in Fig. 1e and Supplementary Fig. 5a), to describe the low frequency ($\omega < 50 \text{ cm}^{-1}$) amplitude contrast measured in $\text{Bi}_2\text{Te}_{2.2}\text{Se}_{0.8}$, we have to include a finite contribution from TSS to the near-field amplitude (see red traces in Fig. 1e and Supplementary Fig. 5a).

Detectorless near-field nanoscopy: role of the topological surface states. With the aim of isolating the nature of the modes activated through THz photoexcitation and their interaction with TSS, we then perform self-detection nanoscopy on a set of flakes with a progressively reduced thickness, employing single-frequency mode THz-quantum cascade lasers (QCLs)¹⁴ as sketched in Fig. 2a, operating at three different emission frequencies, $\omega_0 = 66.7, 76.7, 89.7 \text{ cm}^{-1}$, corresponding to the gray dashed lines in Fig. 1c–e. THz-QCLs have the inherent advantage to provide mW output powers

and high spectral purity, with intrinsic linewidths as low as 100 Hz⁵²; this allows for selective interaction with THz resonant modes. In our self-detection experiment¹⁴, the QCL acts simultaneously as a powerful THz source and as a phase-sensitive detector, employing a detection scheme based on self-mixing (SM) interferometry⁵³, therefore overcoming the need for bulky cryogenic detectors. This effect is based on the reinjection of a small fraction (10^{-4} – 10^{-2}) of the emitted field that coherently interferes within the laser cavity. The fraction of the laser radiation backscattered from the tip-sample system can be coupled back into the QCL cavity along the same optical path. The coherent superposition of reinjected THz field with the QCL intracavity field produces a perturbation of the laser voltage ΔV that depends on both the amplitude and the phase of the THz field scattered by the tip.

s-SNOM experiments allow to excite collective modes of finite momentum by measuring the local response, which is given by the superposition of different modes with a distribution of momenta extended up to $q \sim 1/r$, rather than by a single-mode. Exploiting the higher power and sensitivity of the self-detection experiment with respect to the TDS system, we use a tip with a smaller radius, $r = 10$ nm, corresponding to a spatial resolution of about 30 nm (see Supplementary Fig. 8) and to a larger probed momentum range.

In order to sample the SM fringes and retrieve the phase shift experienced by the field in the scattering process, the length L of the external cavity, formed by the tip and output laser facet, is varied up to 350 μm ($>2\lambda = 4\pi c/\omega_0$) with a delay line built on a linear translation stage with sub- μm spatial resolution (Fig. 2a).

A variable attenuator with transmission t is inserted in the optical path to reduce the optical feedback to the weak limit in which ΔV has a simple sinusoidal dependence on L , expressed, within the framework of the Lang-Kobayashi model⁵⁴, as $\Delta V \sim s \cos(\frac{2\omega_0 L}{c} - \phi)$, with s signal amplitude and ϕ phase of the scattered field. Lock-in detection of the n th harmonics of the tapping frequency Ω is then used to isolate the near-field component from the scattering background. Using a lock-in detection technique we have a noise level of 0.1 μV and a SNR > 40 on the $n = 5$ harmonics on thick flakes.

The scattering signal at the highest harmonic order ($n = 5$), acquired keeping fixed the cavity length L , is enhanced at the flakes compared to the substrate, see Fig. 2d, e. For thicker flakes with $d > 40$ nm, the amplitude of s_5 appears higher for $\text{Bi}_2\text{Te}_{2.2}\text{Se}_{0.8}$ (B1–B2 in Fig. 2c) than for Bi_2Se_3 (A1–A2 in Fig. 2b) in agreement with the η_{Au} values extracted via hyperspectral THz nano-imaging (Fig. 1c). However, the two materials show a different dependence on thickness: while negligible amplitude variation is observed upon reducing the thickness of Bi_2Se_3 from 86 nm (flake A1) to 16 nm (A4) (see Fig. 2d), the s_5 amplitude drops in $\text{Bi}_2\text{Te}_{2.2}\text{Se}_{0.8}$ such that the 19 nm thick flake (B4) is barely distinguishable from the substrate (Fig. 2e).

We then extract line profiles from the maps in Fig. 2b, e while moving along a line orthogonal to the flakes edge and keeping fixed the cavity length L , to show the variation of the substrate/flake contrast with thickness in the two material systems (Fig. 2f, g).

The thickness-dependent signal change, revealed in the line profiles (Fig. 2f, g), could be caused by both a phase shift and by an actual variation of the amplitude of the SM fringes. To discriminate between the two effects, we resolve the phase of the scattered field (predicted in Fig. 1d): we acquire the SM fringes with 0.2 μm steps while scanning the sample along a line orthogonal to the substrate-flake edge. Figure 3a shows the retrieved amplitude signal at the third demodulation order s_3 , as a function of L and of the position on the sample labeled as X.

Considering the drop in the scattering efficiency of the tip with increasing THz frequencies, we choose the third-order demodulated signal s_3 to compare the data collected at the three different

frequencies ω_0 . By analyzing the SM fringes at each X with sinusoidal fit functions (as in Fig. 3b), we extract the amplitude s_3 and the phase ϕ_3 along the scan trajectory (see Supplementary Fig. 9 for the phase profiles).

Since the absolute value of the SM signal depends on the threshold voltage of the THz-QCL, on its output power, and on the frequency-dependent scattering efficiency of the tip, the average scattering signal amplitude from the flake $s_3(\text{flake})$, is divided by the signal from the substrate, $s_3(\text{substrate})$, whose response is expected to show negligible variation with frequency. The refractive index variation of SiO_2 in the 60–90 cm^{-1} range is indeed $<0.5\%$ ⁵⁵. The thickness dependencies of the ratio η_3 , which is accounting for the contrast between flake and substrate, and of the phase change $\Delta\phi_3$, at the three pumping frequencies, are reported in Fig. 3c, e, and in Fig. 3d, f, for Bi_2Se_3 and $\text{Bi}_2\text{Te}_{2.2}\text{Se}_{0.8}$, respectively. The near-field response appears very different in the two materials.

In Bi_2Se_3 , the flat topography regions show roughly constant contrast with the SiO_2 substrate changing the flake thickness d , at all the probing frequencies, while only the signal at the flake edges varies with thickness. Looking at $s_3(\omega_0)$, by keeping fixed the layer thickness, the contrast η_3 increases by 30–40% while increasing ω_0 from $\omega_0 = 66.7 \text{ cm}^{-1}$ to $\omega_0 = 76.7 \text{ cm}^{-1}$ in Bi_2Se_3 (Fig. 3c). This is in disagreement with the calculated 2D near-field response of Bi_2Se_3 that predicts³⁰ a peak in the s_3 amplitude at the TO phonon wavenumber $\omega_{\text{to}}^{\perp} = 64 \text{ cm}^{-1}$ and a strong decrease of about 40% in the range 65–90 cm^{-1} . On the other hand, the observed increase of s_3 is compatible with the overall increase in the same range shown by the calculated contrast in Fig. 1e, and hence suggests a bulk phonon-like nature for the dielectric response of our Bi_2Se_3 samples, in agreement with what emerged from previous reports⁵⁶. On the contrary, $\text{Bi}_2\text{Te}_{2.2}\text{Se}_{0.8}$ exhibits a visible decrease in the scattering intensity with flake thickness d at $\omega_0 = 66.7 \text{ cm}^{-1}$ and $\omega_0 = 76.7 \text{ cm}^{-1}$, which becomes less pronounced at $\omega_0 = 89.7 \text{ cm}^{-1}$, such that, in all cases, the flakes become barely distinguishable ($\eta_3 \sim 1$) from the substrate when $d < 20$ nm (Fig. 3d). The thickness and frequency dependences of s_3 from $\text{Bi}_2\text{Te}_{2.2}\text{Se}_{0.8}$ are consistent with a recent model³⁰ of the near-field response formulated for Bi_2Se_3 which predicts deeply sub-diffractive, highly directional hyperbolic phonon-polaritons interacting with the electrons of the TSS. In particular, the experimental frequency dependence of $\text{Bi}_2\text{Te}_{2.2}\text{Se}_{0.8}$ is retrieved if one includes a red-shift of the spectral features predicted by the model for Bi_2Se_3 towards the optical phonon frequencies of Bi_2Te_3 to describe $\text{Bi}_2\text{Te}_{2.2}\text{Se}_{0.8}$, whose phonon frequencies reasonably approaches the ones of Bi_2Te_3 ⁴⁶. A detailed simulation of the near-field response s_3 of Bi_2Te_3 , as a function of the pumping frequency and of the flake thickness, is reported in the Supplementary Information (Supplementary Note 4 and Supplementary Fig. 15a). Consistently, in the $\text{Bi}_2\text{Te}_{2.2}\text{Se}_{0.8}$ flakes (Fig. 3d), $s_3(\omega_0)$ is almost frequency independent in the 66.7 $\text{cm}^{-1} < \omega_0 < 76.7 \text{ cm}^{-1}$ range and then increases when $\omega_0 = 89.7 \text{ cm}^{-1}$, as we approach the peak of s_3 due to the TO phonon at $\omega_{\text{to}}^{\parallel} = 95 \text{ cm}^{-1}$.

A strong and sharp peak in near-field contrast is predicted at $\omega_{\text{to}}^{\perp}$ ³⁰, that in a $\text{Bi}_2\text{Te}_{2.2}\text{Se}_{0.8}$ falls outside of the investigated spectral range ($\omega_{\text{to}}^{\perp} = 50 \text{ cm}^{-1}$ for the Bi_2Te_3)^{46,47}. However, differently from the peak at $\omega_{\text{to}}^{\parallel}$, this peak is related to the far-field factor rather than to the near-field tip-sample interaction.

Propagating collective excitations. Figure 4 shows the near-field maps (Fig. 4a, b) of the edges of the Bi_2Se_3 and $\text{Bi}_2\text{Te}_{2.2}\text{Se}_{0.8}$ flakes, acquired at $\omega_0 = 66.7 \text{ cm}^{-1}$ for a fixed cavity length L , and the related line profiles extracted by averaging over the displayed window along the vertical axis (Fig. 4c, d).

Analogous line profiles measured at $\omega_0 = 76.7$ and 90 cm^{-1} are reported in Supplementary Figs. 10, 11.

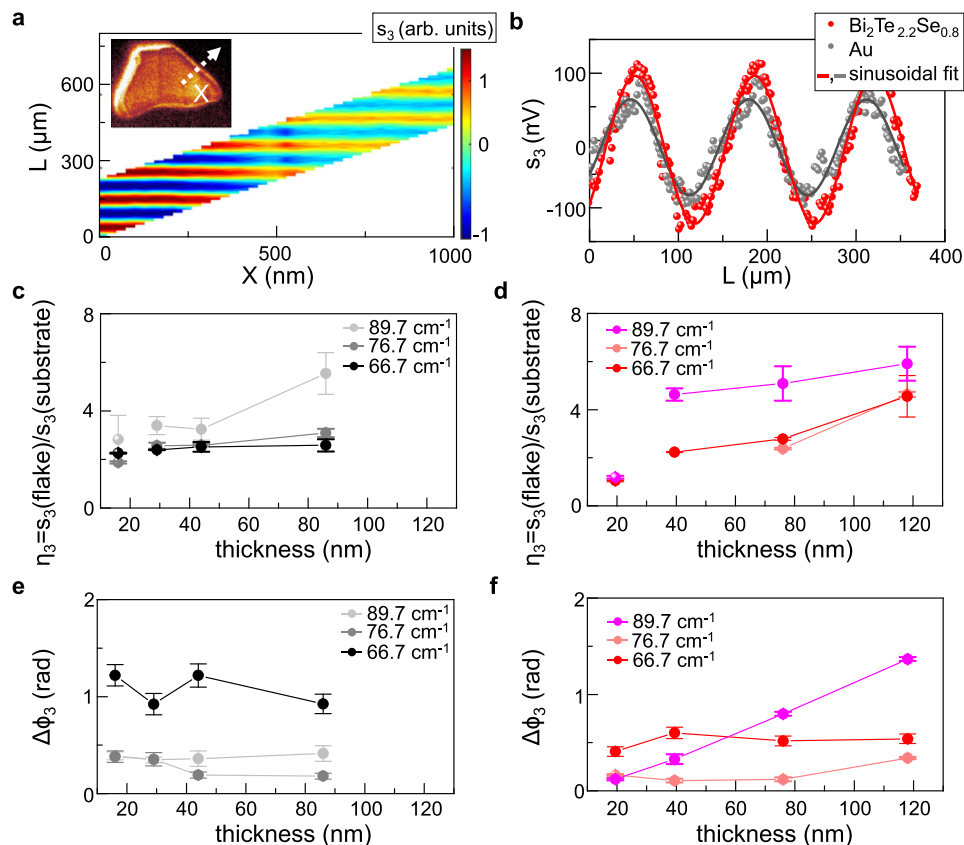


Fig. 3 Amplitude and phase contrasts. **a** SM maps of s_3 signal on flake A2 of Bi_2Se_3 as a function of the cavity length L and of the position X moving on the line orthogonal to the flake edge sketched in the inset by the white dashed arrow; the L sampling interval changes with X due to the delay line backlash. **b** SM fringes of s_3 as a function of the cavity length L at a fixed position X on flake B3 of $\text{Bi}_2\text{Te}_{2.2}\text{Se}_{0.8}$ (red dots) and on the substrate (gray dots) acquired at 76.7 cm^{-1} together with the sinusoidal best fit (solid lines). **c, d** Signal contrast η_3 evaluated dividing the signal amplitude s_3 on Bi_2Se_3 (**c**) and on $\text{Bi}_2\text{Te}_{2.2}\text{Se}_{0.8}$ (**d**) by that collected on the substrate, all extracted from the sinusoidal fit of the SM fringes acquired on $1\text{-}\mu\text{m}$ -length X line scan across the flake/substrate interface, measured at three different probing frequencies. Error bars indicate 95% confidence bands from the fit. **e, f** Phase variation $\Delta\phi_3$ from the substrate to the flakes, extracted from the sinusoidal fit of the SM fringes acquired on $1\text{-}\mu\text{m}$ -length X line scan across the flake/substrate interface, as a function of the flake thickness at the three different frequencies for Bi_2Se_3 (**e**) and $\text{Bi}_2\text{Te}_{2.2}\text{Se}_{0.8}$ (**f**). Error bars indicate 95% confidence bands from the fit.

The near-field scattering maps (Fig. 4a, b) show a visible signal enhancement at the flake edges with the brightest edge corresponding to the side from which the THz beam enters in the s-SNOM.

A strong signal enhancement at the flakes edges has been previously identified in hBN as a signature of the activation of localized phonon-polariton modes⁵⁷. The peaks localized at the flake edges have distinct thickness dependence in the two materials: in Bi_2Se_3 the peak broadens and increases its intensity with the thickness (Fig. 4c), while it appears always sharper, and with a less pronounced dependence of intensity on thickness in the $\text{Bi}_2\text{Te}_{2.2}\text{Se}_{0.8}$ (Fig. 4d). We ascribe those peaks to edge resonances of phonon-polariton modes⁵⁷, whose interplay with the main photoexcited modes quickly damps them close to the edge. Indeed, while the peaks retrieved in Fig. 4c, d are visibly edge modes, we observe signal intensity modulations in regions on flat topography (Fig. 4c, d), characterized by a much weaker amplitude, which we attribute to the interference of propagating modes launched by the tip and reflected at the flake edges. In our case, these oscillations in Bi_2Se_3 have comparable amplitude changing the thickness, while in $\text{Bi}_2\text{Te}_{2.2}\text{Se}_{0.8}$ they display a less pronounced intensity for thinner flakes, becoming not distinguishable in the thinner flake ($d = 19\text{ nm}$).

To unveil the nature of the aforementioned propagating photoexcited modes, we analyze these signal oscillations with the function: $s_3(x) = \text{Re}\left(\frac{A}{\sqrt{x-x_0}} e^{2iq_p(x-x_0)}\right) + B$, expected for modes launched by the tip and reflected by the flake edges⁵⁸. In the fitting function, A is a complex-valued amplitude, B is a constant background, x_0 represents the position of the reflecting interface taken as the flakes' edge (dashed line in Fig. 4c, d), $1/\sqrt{x-x_0}$ is the geometrical decay and the exponential describes oscillations with periodicity $\frac{\pi}{q_p}$, where the wavevector q_p is complex-valued $q_p = q_1 + iq_2$. The double period $\lambda_p = \frac{2\pi}{q_1}$ represents the wavelength of the photoexcited modes, whose frequency is set by the energy conservation law to match that of the impinging photon⁵⁹.

Figure 5a shows the obtained λ_p as a function of the flake thickness for Bi_2Se_3 and $\text{Bi}_2\text{Te}_{2.2}\text{Se}_{0.8}$, respectively, at the three probed frequencies. In Bi_2Se_3 , λ_p is almost thickness independent (Fig. 5a) at all probing frequencies. Vice versa in $\text{Bi}_2\text{Te}_{2.2}\text{Se}_{0.8}$, there is a visible dependence of the oscillation period on d (Fig. 5b): λ_p decreases while reducing d .

The thickness-independent trend, extrapolated in Bi_2Se_3 , is compatible with photoexcited massive plasmons formed by the bulk charge carriers at the flakes surface, which give rise to a

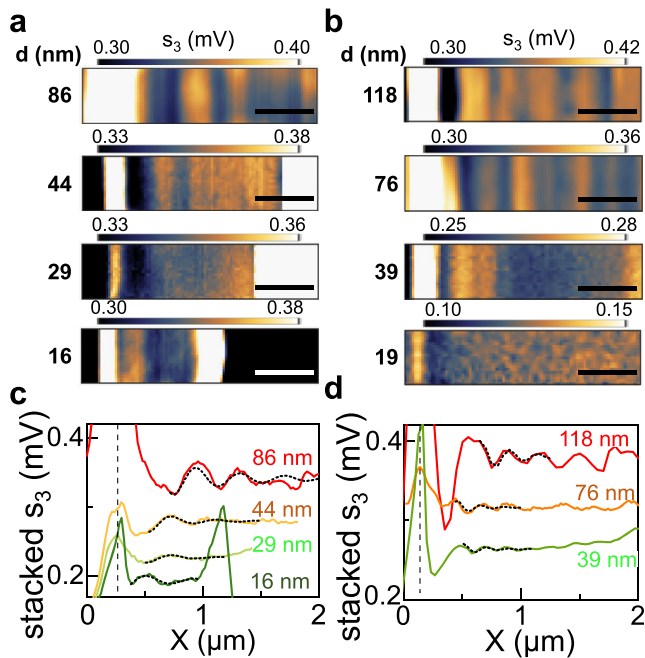


Fig. 4 Real-space mapping of propagating excitations. **a, b** Near-field scattering maps of s_3 acquired at 66.7 cm^{-1} at the edge of Bi_2Se_3 (**a**) and $\text{Bi}_2\text{Te}_{2.2}\text{Se}_{0.8}$ (**b**) flakes, with different thicknesses d , indicated on the side. The scale bar corresponds to 500 nm. **c, d** Line profiles (colored solid lines) extracted averaging the maps in panels **a, b** vertically on the displayed window, showing signal oscillations as a function of the position X on flakes of Bi_2Se_3 (**c**) and $\text{Bi}_2\text{Te}_{2.2}\text{Se}_{0.8}$ (**d**). The line profile corresponding to the map of the 19-nm-thick flake of $\text{Bi}_2\text{Te}_{2.2}\text{Se}_{0.8}$ is not reported because it lacks evident periodicity. The line profiles are aligned to have the highest peak at the same position, which is identified by the black dashed vertical line. Fits of the oscillations to extract the periodicity, performed with the function described in the text, are plotted as short-dot black lines.

2DEG, as a consequence of the band bending at the Bi_2Se_3 interface with adjacent materials³⁶.

Conversely, the extrapolated thickness dependence of λ_p in $\text{Bi}_2\text{Te}_{2.2}\text{Se}_{0.8}$ is expected either in presence of massive plasmons related to bulk charge carriers or for Dirac plasmons related to TSS^{56,60}. It is worth mentioning that, in the limit of small wavevectors ($qd < 1$), Dirac plasmons dispersion can be approximated to the thickness-independent first-order dispersion⁸, while at larger wavevectors both the dependence on the thickness and on the bulk dielectric function emerge^{60,61}.

We then investigate the experimental mode dispersion (Fig. 5c, d), for both material systems, and compare it with the theoretical trends predicted under the hypothesis discussed above. A quadratic dependence of the real part of the wavevector $q_1 = 2\pi/\lambda_p$ on the frequency $\omega_p = \omega_0$ is observed for both materials. In Bi_2Se_3 the dispersion curve, calculated for massive plasmons formed by the 2DEG charge carriers³⁶, perfectly matches our experimental data (Fig. 5c), confirming our claim. The dispersion of massive plasmons³⁰ is evaluated using the relation $\omega_p^2 = \frac{e^2}{2\epsilon_0 \epsilon_r} \frac{n_M}{m_{\text{eff}}} q_1$, where $\epsilon_r \sim 6.3$ is the average permittivity of the materials surrounding the flake (silica/silicon substrate and air), e is the electron charge, ϵ_0 is the vacuum permittivity, n_M is the carrier density associated with the 2DEG and $m_{\text{eff}} = 0.15 m_0$ is the effective mass³⁴ of Bi_2Se_3 , with m_0 electron mass. Good agreement with the data is obtained considering a surface carrier density $n_M = 3 \times 10^{10} \text{ cm}^{-2}$, which indicates charge-carrier depletion at the surface, in agreement with previous studies^{62,63} on Bi_2Se_3 .

The theoretical dispersion curves predicted in $\text{Bi}_2\text{Te}_{2.2}\text{Se}_{0.8}$ for massive bulk plasmons and for TSS Dirac plasmons are shown in

Supplementary Fig. 12a, b, respectively. In the case of massive bulk plasmons, we use the same dispersion relation as for Bi_2Se_3 massive plasmon but with the effective mass⁶⁴ of Bi_2Te_3 $m_{\text{eff}} = 0.044 m_0$, and a thickness-dependent density for the bulk massive electrons $n_M(d)$. The thickness dependence is here encoded into the carrier density term $n_M = n_s + C \cdot n_{\text{bv}} d^{0.5}$, which depends on the sheet carrier density n_s , on the bulk carrier density n_{bv} , and for which we consider a square-root dependence on the thickness d as in ref. ⁶⁵. A bulk carrier density $n_{\text{bv}} = 3 \times 10^{18} \text{ cm}^{-3}$ in $\text{Bi}_2\text{Te}_{2.2}\text{Se}_{0.8}$ is taken from the value experimentally retrieved with direct Hall measurement in $\text{Bi}_2\text{Te}_{2.4}\text{Se}_{0.6}$ ⁶⁶, the coefficient $C = 0.8 \times 10^{-5} \text{ m}^{0.5}$ is taken from ref. ⁶⁵ and estimation of $n_s = 2 \times 10^{12} \text{ cm}^{-2}$ is obtained by multiplying n_{bv} from ref. ⁶⁶ for the thickness of the flake used for the n_{bv} determination (6 QL~8 nm). On the contrary, the dispersion of Dirac

plasmons associated with TSS^{56,60} is: $\omega_p^2 = \frac{e^2 v_F \sqrt{2\pi n_D}}{h} \frac{q_1}{\epsilon_r + qd\epsilon_{\text{Tl}}}$ where n_D is the Dirac carrier density (assumed equal to n_s to calculate the dispersion), h is the Planck constant, and $\epsilon_{\text{Tl}}(\omega)$ is the Bi_2Te_3 permittivity⁵⁶. The frequency dependence of ϵ_{Tl} is crucial to account for the thickness dependence of the Dirac plasma frequency⁶⁷, while here we use an average of the dielectric constants along the basal plane ϵ^\perp and along the c -axis ϵ^\parallel , computed as: $\epsilon_{\text{Tl}} = \sqrt{\epsilon^\parallel \cdot \epsilon^\perp}$. Our model for the dielectric permittivity of Bi_2Se_3 and Bi_2Te_3 is detailed in Supplementary Note 4. The data of Supplementary Fig. 12a, b indeed clearly show that for Bi_2Te_3 none of these trends matches with our experimental data (Fig. 5d), and that, for both assumptions, we would expect much lower q values. This reflects in propagating plasmon wavelengths λ_p (Supplementary Fig. 12c, d) significantly longer ($>100 \mu\text{m}$), impossible to be captured via near-field nanoscopy.

We cannot, therefore, ascribe the oscillations observed in $\text{Bi}_2\text{Te}_{2.2}\text{Se}_{0.8}$ to propagating bulk plasmons or Dirac plasmons. To shed further light on the nature of these modes we then perform numerical simulations of the collective mode energy dispersion in our $\text{Bi}_2\text{Te}_{2.2}\text{Se}_{0.8}$ flakes, following the procedure described in ref. ³⁰. We look for the dispersion of phonon-polariton modes in the presence of charge carriers populating the TSS, described by the surface sheet conductivity of Dirac fermions⁶⁸, assuming that the chemical potential is located in the bulk bandgap, resulting in a negligible bulk conductance. The charge carriers in the TSS are expected to form Dirac plasmons that hybridize with the phonon-polariton modes to form hyperbolic plasmon-phonon-polaritons.

The near-field signal can be considered as a weighted average of the surface reflectivity for p- (or TM-) polarized light $r_p(q, \omega_0)$ over q . The dispersion of collective modes is identified by the maxima, at real arguments q and ω , of the imaginary part of the $r_p(q, \omega)$, $\text{Im}\{r_p(q, \omega)\}$, which we calculate including the strong anisotropy of the frequency-dependent dielectric permittivity of $\text{Bi}_2\text{Te}_{2.2}\text{Se}_{0.8}$ (see Methods).

The false color maps of the function $\text{Im}\{r_p(q, \omega)\}$ in Fig. 6 provide a convenient visualization of the collective mode spectra.

The bright lines in Fig. 6a–c are the dispersion curves of the collective modes calculated for $\text{Bi}_2\text{Te}_{2.2}\text{Se}_{0.8}$ flakes of different thickness, assuming a constant chemical potential $\mu = 200 \text{ meV}$, which is chosen to fall within the electronic bandgap of the material ($\sim 280 \text{ meV}$ ³⁵). The $\text{Im}\{r_p\}$ map calculated for chemical potentials $\mu = 50 \text{ meV}$, $\mu = 150 \text{ meV}$, and $\mu = 250 \text{ meV}$ and for flake thickness 118 nm is reported in the Supplementary Fig. 14. In bismuth chalcogenide compounds, the electrochemical potential is indeed expected to approach the bottom of the conduction band as a consequence of the doping due to vacancies or antisite defects⁶⁹. The smearing of the dispersion lines gives an idea of how damped the modes are.

The comparison with our experimental data (white crosses in Fig. 6a–c), show that our photoexcited modes all falls in the upper half of the hyperbolic band $\omega_{\text{to}}^\perp < \omega < \omega_{\text{to}}^\parallel$ and their q values correspond to those expected for hybrid modes resulting from

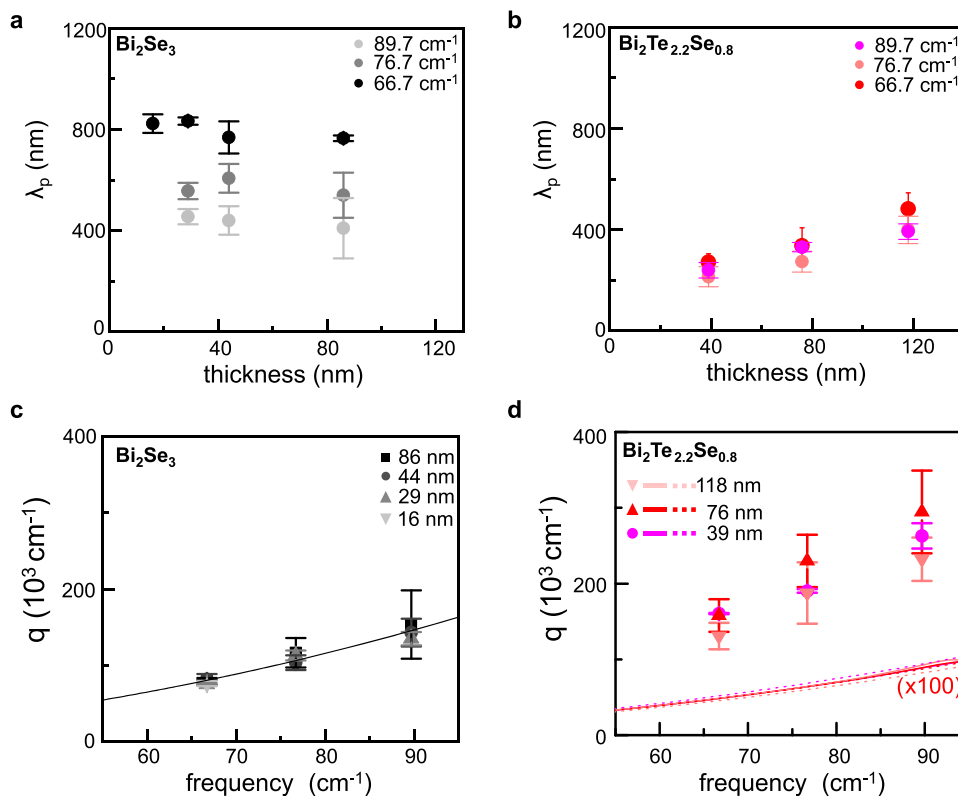


Fig. 5 Energy dispersions of propagating modes. **a** Plasmon wavelength λ_p in Bi_2Se_3 as a function of thickness, extracted from the interference pattern measured at 66.7 cm^{-1} (black dots), at 76.7 cm^{-1} (gray dots), and at 89.7 cm^{-1} (light gray dots). **b** Wavelength λ_p of the photoexcited modes in $\text{Bi}_2\text{Te}_{2.2}\text{Se}_{0.8}$ as a function of flake thickness extracted from the interference pattern measured at 66.7 cm^{-1} (red dots), at 76.7 cm^{-1} (light red dots), and 89.7 cm^{-1} (magenta dots). **c** Plasmon energy dispersion in Bi_2Se_3 for different flake thicknesses d ranging from 86 to 16 nm (colored dots) together with the predicted dispersion law (solid line). **d** Energy dispersion of the photoexcited modes in $\text{Bi}_2\text{Te}_{2.2}\text{Se}_{0.8}$ for different flake thicknesses d ranging from 118 to 39 nm (colored dots), compared to the energy dispersion simulated for Dirac plasmons (colored solid lines) and massive bulk plasmons (colored dot lines) reported in Supplementary Fig. 12 and therein-discussed in detail. Error bars indicate the 95% confidence bands from the fit of interference patterns.

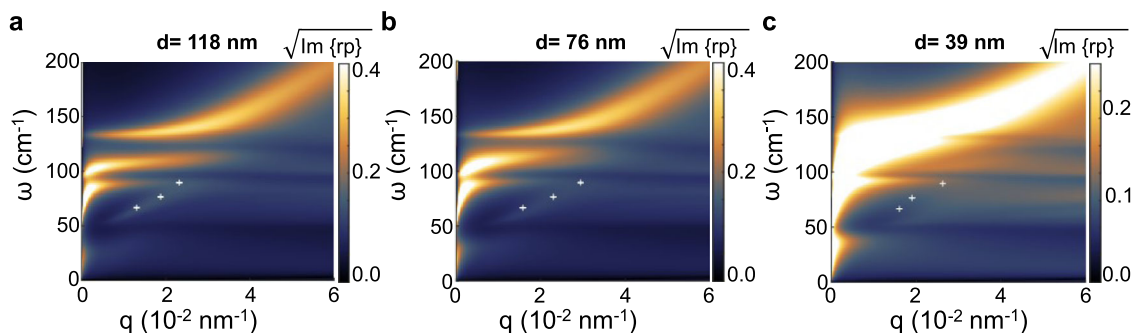


Fig. 6 Collective mode dispersions. **a–c** Collective mode dispersions of Bi_2Te_3 slabs of different thickness d , rendered using the false color maps of $\text{Im}\{r_p\}$. The parameters of the calculation are $\mu = 0.2\text{ eV}$ and **a** $d = 118\text{ nm}$; **b** $d = 76\text{ nm}$; **c** $d = 39\text{ nm}$. In the plots, the Fermi velocity is $v_F = 0.5 \times 10^8\text{ cm/s}$ as for Bi_2Te_3 from ref. 48, the electron scattering rate is $\gamma_e = 1\text{ THz}$ as in ref. 4, the vacuum and substrate permittivity are $\epsilon_0 = 1$, and $\epsilon_{\text{sub}} = 6.3$. The white symbols correspond to the experimental data of Fig. 5d.

hybridization of hyperbolic phonon-polaritons with TSS Dirac plasmons into combined hyperbolic plasmon-phonon-polaritons modes (HP³ modes), and differ significantly from those expected when only Dirac plasmons come into play (see Supplementary Fig. 12b). The effect of the hybridization is encoded in the frequency shift of the dispersion curves when there is finite doping (see Supplementary Fig. 14). The damping of these modes is a consequence of the strong electron interaction with the charge carriers and increases with doping. From Fig. 6 we can also observe that the hyperbolic phonon-polariton modes fade away while decreasing the flake thickness. It is worth mentioning

that the carrier density plays a fundamental role in dictating the observable activated excitations in our geometry, i.e., with wavelengths within the physical size of the exfoliated flakes. Indeed, in the case of Bi_2Se_3 , the expected lower surface carrier density, combined with the larger effective mass m_{eff} , entails the activation of short wavelength λ_p (submicron) massive plasmons, whereas these are not observable in $\text{Bi}_2\text{Te}_{2.2}\text{Se}_{0.8}$ because the higher carrier density and lower m_{eff} push λ_p in the 0.5–1 mm range. Therefore, the ability to controllably tune the carrier density, e.g., by electrostatic gating, could open the possibility to selectively ignite the different phenomena.

Analogous activation of mixed plasmon and hyperbolic phonon-polaritons has been predicted for hBN thin slabs³⁰, with the difference that the hyperbolic bands of hBN fall in the mid-infrared range, at much higher frequencies (around 1500 cm⁻¹). Technological applications based on mid-infrared hyperbolic phonon-polaritons demonstrated for hBN, such as hyperlensing⁷⁰, waveguiding³⁰, and light focusing⁷¹, can be translated to the THz frequency range using Bi₂Te_{2.2}Se_{0.8} flakes. The hybridization of phonon-polaritons with Dirac plasmons introduces additional control knobs, namely flake thickness and doping, to tune the HP³ mode dispersion and accordingly the THz response of Bi₂Te_{2.2}Se_{0.8} flakes. Moreover, since HP³ modes are highly directional³⁰, a change in the doping can be exploited to vary the propagation direction of the HP³.

In conclusion, we have provided the first direct experimental evidence of hyperbolic plasmon-phonon-polaritons modes at THz frequencies, and of the activation of massive bulk plasmons associated to band bending induced 2DEG, providing novel insights on the rich physics of TI materials. The interaction of the probed phonon-polaritons modes with the electrons from the TSS suggests possible ultrafast optical control¹⁶ by above bandgap photoexcitation to ideally switch on and off the hybridized modes, opening intriguing technological perspectives in plasmonics⁷², ultrafast photonics, spintronics¹⁰, nanophotonics^{73,74}, and quantum optics⁷⁵.

Methods

Growth. Single-crystalline ingots of Bi₂Se₃ and Bi₂Te_{2.2}Se_{0.8} were grown from melt by the vertical vacuum/inert atmosphere optimized Bridgman–Stockbarger method, following methods described in ref. ⁷⁶. The resulting samples show extremely high chemical stability and do not manifest any effect related to degradation under air exposure.

Total reflectivity of Bi₂Te_{2.2}Se_{0.8}. The sample system is modeled as a stack of three materials: the air superstrate (labeled as 0) with permittivity $\epsilon_0 = 1$, from which the incident THz beam comes, the Bi₂Te_{2.2}Se_{0.8} flake of thickness d (labeled as 1) with sheet conductivity, $\sigma_{SS}(q, \omega)$ and the undoped silicon/silica substrate (labeled as 2) with permittivity $\epsilon_s = 6.3$. Following ref. ³⁰, the P-polarization reflectivity r_P of this layered system is given by:

$$r_P = \frac{r_{12}(r_{01} + r_{10} - 1) - r_{01}e^{-2ik_{//}d}}{r_{10}r_{12} - e^{-2ik_{//}d}} \quad (1)$$

where $k_{//} = \sqrt{\epsilon^{\perp} \sqrt{\frac{\omega^2}{c^2} - \frac{q^2}{\epsilon^{\parallel}}}}$ is the out-of-plane momentum inside the flake, and ϵ^{\perp} and ϵ^{\parallel} are the in-plane and out-of-plane dielectric permittivities calculated from the parameters available in the literature for Bi₂Te₃ as detailed in the supplementary information. The term r_{12} is the reflectivity at the flake/substrate interface and r_{01} , r_{10} are the reflectivities at the air/flake interface as coming from the air and from the flake side, respectively. These latter are computed as follows in cgs units:

$$\begin{aligned} r_{01} &= \frac{\epsilon^{\perp}k_0 - \epsilon_0k_{//} + \frac{4\pi}{\omega}\sigma_{SS}k_0k_{//}}{\epsilon^{\perp}k_0 + \epsilon_0k_{//} + \frac{4\pi}{\omega}\sigma_{SS}k_0k_{//}}; \\ r_{10} &= \frac{\epsilon_0k_{//} - \epsilon^{\perp}k_0 + \frac{4\pi}{\omega}\sigma_{SS}k_{//}k_0}{\epsilon_0k_{//} + \epsilon^{\perp}k_0 + \frac{4\pi}{\omega}\sigma_{SS}k_{//}k_0}; \\ r_{12} &= \frac{\epsilon_s k_{//} - \epsilon^{\perp}k_s + \frac{4\pi}{\omega}\sigma_{SS}k_s k_{//}}{\epsilon_s k_{//} + \epsilon^{\perp}k_s + \frac{4\pi}{\omega}\sigma_{SS}k_s k_{//}} \end{aligned} \quad (2)$$

k_s and k_0 are the out-of-plane momenta at the substrate and in the air and are defined in analogy to that in the flake but considering that they are isotropic materials: $k_s = \sqrt{\epsilon_s} \sqrt{\frac{\omega^2}{c^2} - \frac{q^2}{\epsilon_s}}$ and $k_0 = \sqrt{\frac{\omega^2}{c^2} - q^2}$. Finally, the sheet conductivity σ_{SS} is evaluated as:

$$\sigma_{SS} = \frac{i\omega}{q^2} e^2 P$$

with P polarizability of Dirac fermions^{30,68}, in which the Fermi velocity of the material $v_F = 0.5 \times 10^8$ cm/s and the chemical potential μ enter.

By using the same σ_{SS} in r_{01} and in r_{12} we are assuming the same sheet conductivity at both the interfaces air/flake and flake/substrate. The sheet conductivity is nonzero only for finite doping and determines the appearance of the Dirac plasmon modes and their hybridization with hyperbolic phonon-polaritons to form HP³ excitations.

Data availability

The data that support the plots within this paper and other findings of this study are available from the corresponding authors upon reasonable request.

Code availability

The codes and simulation files that support the plots and data analysis within this paper are available from the corresponding author upon reasonable request.

Received: 18 June 2021; Accepted: 25 October 2021;

Published online: 18 November 2021

References

- Moore, J. E. The birth of topological insulators. *Nature* **464**, 194–198 (2010).
- Hasan, M. Z. & Kane, C. L. Colloquium: topological insulators. *Rev. Mod. Phys.* **82**, 3045–3067 (2010).
- Zhang, X., Wang, J. & Zhang, S.-C. C. Topological insulators for high-performance terahertz to infrared applications. *Phys. Rev. B Condens. Matter Mater. Phys.* **82**, 245107 (2010).
- Shao, J. M., Li, H. & Yang, G. W. Warping effect-induced optical absorbance increment of topological insulator films for THz photodetectors with high signal-to-noise ratio. *Nanoscale* **6**, 3513–3517 (2014).
- Zhang, T., Ha, J., Levy, N., Kuk, Y. & Stroscio, J. Electric-field tuning of the surface band structure of topological insulator Sb₂Te₃ thin films. *Phys. Rev. Lett.* **111**, 056803 (2013).
- Viti, L. et al. Plasma-wave terahertz detection mediated by topological insulators surface states. *Nano Lett.* **16**, 80–87 (2016).
- Politano, A. et al. Interplay of surface and Dirac plasmons in topological insulators: the case of Bi₂Se₃. *Phys. Rev. Lett.* **115**, 216802 (2015).
- Di Pietro, P. et al. Observation of Dirac plasmons in a topological insulator. *Nat. Nanotechnol.* **8**, 556–560 (2013).
- Kitaev, A. & Preskill, J. Topological entanglement entropy. *Phys. Rev. Lett.* **96**, 110404 (2006).
- Chen, Y. L. et al. Experimental realization of a three-dimensional topological insulator, Bi₂Te₃. *Science* **325**, 178–181 (2009).
- Fei, Z. et al. Gate-tuning of graphene plasmons revealed by infrared nano-imaging. *Nature* **486**, 82–85 (2012).
- Chen, J. et al. Optical nano-imaging of gate-tunable graphene plasmons. *Nature* **487**, 77–81 (2012).
- Ni, G. X. et al. Ultrafast optical switching of infrared plasmon polaritons in high-mobility graphene. *Nat. Photonics* **10**, 244–247 (2016).
- Giordano, M. C. et al. Phase-resolved terahertz self-detection near-field microscopy. *Opt. Express* **26**, 18423–18435 (2018).
- Dai, S. et al. Tunable phonon polaritons in atomically thin van der Waals crystals of boron nitride. *Science* **343**, 1125–1129 (2014).
- Huber, M. A. et al. Femtosecond photo-switching of interface polaritons in black phosphorus heterostructures. *Nat. Nanotechnol.* **12**, 207–211 (2017).
- Stockbarger, D. C. The production of large single crystals of lithium fluoride. *Rev. Sci. Instrum.* **7**, 133–136 (1936).
- Bridgman, P. W. Certain physical properties of single crystals of tungsten, antimony, bismuth, tellurium, cadmium, zinc, and tin. *Proc. Am. Acad. Arts Sci.* **60**, 305–383 (1925).
- Keilmann, F., Huber, A. J. & Hillenbrand, R. Nanoscale conductivity contrast by scattering-type near-field optical microscopy in the visible, infrared and THz domains. in *J. Infrared, Millim., Terahertz Waves* **30**, 1255–1268 (2009). Springer.
- Amarie, S. & Keilmann, F. Broadband-infrared assessment of phonon resonance in scattering-type near-field microscopy. *Phys. Rev. B Condens. Matter Mater. Phys.* **83**, 045404 (2011).
- Hegenbarth, R. et al. High-power femtosecond mid-IR sources for s-SNOM applications. *J. Opt.* **16**, 094003 (2014).
- Knoll, B. et al. Contrast of microwave near-field microscopy. *Appl. Phys. Lett.* **70**, 2667–2669 (1997).
- Liewald, C. et al. All-electronic terahertz nanoscopy. *Optica* **5**, 159–163 (2018).
- Schnell, M. et al. Amplitude- and phase-resolved near-field mapping of infrared antenna modes by transmission-mode scattering-type near-field microscopy. *J. Phys. Chem. C* **114**, 7341–7345 (2010).
- Ocelic, N., Huber, A. & Hillenbrand, R. Pseudoheterodyne detection for background-free near-field spectroscopy. *Appl. Phys. Lett.* **89**, 101124 (2006).
- Smith, D. R. & Schurig, D. Electromagnetic wave propagation in media with indefinite permittivity and permeability tensors. *Phys. Rev. Lett.* **90**, 077405 (2003).
- Podolskiy, V. A. & Narimanov, E. E. Strongly anisotropic waveguide as a nonmagnetic left-handed system. *Phys. Rev. B Condens. Matter Mater. Phys.* **71**, 201101 (2005).

28. Caldwell, J. D. et al. Sub-diffractive volume-confined polaritons in the natural hyperbolic material hexagonal boron nitride. *Nat. Commun.* **5**, 5221 (2014).
29. Yoxall, E. et al. Direct observation of ultraslow hyperbolic polariton propagation with negative phase velocity. *Nat. Photonics* **9**, 674–678 (2015).
30. Wu, J. S., Basov, D. N. & Fogler, M. M. Topological insulators are tunable waveguides for hyperbolic polaritons. *Phys. Rev. B Condens. Matter Mater. Phys.* **92**, 205430 (2015).
31. Aghamiri, N. A. et al. Hyperspectral time-domain terahertz nano-imaging. *Opt. Express* **27**, 24231–24242 (2019).
32. Black, J., Conwell, E. M., Seigle, L. & Spencer, C. W. Electrical and optical properties of some $M_2V-BN_3^{VI-B}$ semiconductors. *J. Phys. Chem. Solids* **2**, 240–251 (1957).
33. Walsh, L. A. et al. Fermi level manipulation through native doping in the topological insulator Bi_2Se_3 . *ACS Nano* **12**, 6310–6318 (2018).
34. Bansal, N. et al. Thickness-independent transport channels in topological insulator Bi_2Se_3 thin films. *Phys. Rev. Lett.* **109**, 116804 (2012).
35. Greenaway, D. L. & Harbeck, G. Band structure of bismuth telluride, bismuth selenide and their respective alloys. *J. Phys. Chem. Solids* **26**, 1585–1604 (1965).
36. Bianchi, M. et al. Coexistence of the topological state and a two-dimensional electron gas on the surface of Bi_2Se_3 . *Nat. Commun.* **1**, 128 (2010).
37. Steinberg, H., Gardner, D. R., Lee, Y. S. & Jarillo-Herrero, P. Surface state transport and ambipolar electric field effect in Bi_2Se_3 nanodevices. *Nano Lett.* **10**, 5032–5036 (2010).
38. Cai, S. et al. Independence of topological surface state and bulk conductance in three-dimensional topological insulators. *npj Quantum Mater.* **3**, 1–6 (2018).
39. Qu, D. X., Hor, Y. S., Xiong, J., Cava, R. J. & Ong, N. P. Quantum oscillations and Hall anomaly of surface states in the topological insulator Bi_2Te_3 . *Science* **329**, 821–824 (2010).
40. Horák, J., Sary, Z., Lošťák, P. & Pancf, J. Anti-site defects in n- Bi_2Se_3 crystals. *J. Phys. Chem. Solids* **51**, 1353–1360 (1990).
41. Brahlek, M., Koirala, N., Bansal, N. & Oh, S. Transport properties of topological insulators: band bending, bulk metal-to-insulator transition, and weak anti-localization. *Solid State Commun.* **215–216**, 54–62 (2015).
42. Nechaev, I. A. et al. Evidence for a direct band gap in the topological insulator Bi_2Se_3 from theory and experiment. *Phys. Rev. B* **87**, 121111 (2013). (R).
43. Slocum, D. M., Slingerland, E. J., Giles, R. H. & Goyette, T. M. Atmospheric absorption of terahertz radiation and water vapor continuum effects. *J. Quant. Spectrosc. Radiat. Transf.* **127**, 49–63 (2013).
44. Mastel, S. et al. Terahertz nanofocusing with cantilevered terahertz-resonant antenna tips. *Nano Lett.* **17**, 6526–6533 (2017).
45. Von Ribbeck, H.-G. et al. Spectroscopic THz near-field microscope. *Opt. Express* **16**, 3430–3438 (2008).
46. Richter, W. & Becker, C. R. A Raman and far-infrared investigation of phonons in the rhombohedral V_2-VI_3 compounds Bi_2Te_3 , Bi_2Se_3 , Sb_2Te_3 and $Bi_2(Te_{1-x}Se_x)_3$. *Phys. Status Solidi B* **84**, 619–628 (1977).
47. Boulares, I. et al. Surface phonons in the topological insulators Bi_2Se_3 and Bi_2Te_3 . *Solid State Commun.* **271**, 1–5 (2018).
48. Reijnders, A. A. et al. Optical evidence of surface state suppression in Bi-based topological insulators. *Phys. Rev. B Condens. Matter Mater. Phys.* **89**, 075138 (2014).
49. Cvitkovic, A., Ocelic, N. & Hillenbrand, R. Analytical model for quantitative prediction of material contrasts in scattering-type near-field optical microscopy. *Opt. Express* **15**, 8550–8565 (2007).
50. Schneider, S. C., Grafström, S. & Eng, L. M. Scattering near-field optical microscopy of optically anisotropic systems. *Phys. Rev. B Condens. Matter Mater. Phys.* **71**, 115418 (2005).
51. Mooshammer, F. et al. Nanoscale near-field tomography of surface states on $(Bi_{0.5}Sb_{0.5})_2Te_3$. *Nano Lett.* **18**, 7515–7523 (2018).
52. Vitiello, M. S., Scalari, G., Williams, B. & De Natale, P. Quantum cascade lasers: 20 years of challenges. *Opt. Express* **23**, 5167 (2015).
53. Rakić, A. D. et al. Sensing and imaging using laser feedback interferometry with quantum cascade lasers. *Appl. Phys. Rev.* **6**, 021320 (2019).
54. Lang, R. & Kobayashi, K. External optical feedback effects on semiconductor injection laser properties. *IEEE J. Quantum Electron* **16**, 347–355 (1980).
55. Molster, K. M. *THz Time Domain Spectroscopy of Materials in Reflection and Transmission*. MSc thesis, Nor. Univ. Sci. Technol. (2017).
56. Deshko, Y., Krusin-Elbaum, L., Menon, V., Khanikaev, A. & Trevino, J. Surface plasmon polaritons in topological insulator nano-films and superlattices. *Opt. Express* **24**, 7398–7410 (2016).
57. Babicheva, V. E., Gamage, S., Stockman, M. I. & Abate, Y. Near-field edge fringes at sharp material boundaries. *Opt. Express* **25**, 23935–23944 (2017).
58. Dai, S. et al. Efficiency of launching highly confined polaritons by infrared light incident on a hyperbolic material. *Nano Lett.* **17**, 5285–5290 (2017).
59. Lundberg, M. B. et al. Thermoelectric detection and imaging of propagating graphene plasmons. *Nat. Mater.* **16**, 204–207 (2017).
60. Stauber, T., Gómez-Santos, G. & Brey, L. Spin-charge separation of plasmonic excitations in thin topological insulators. *Phys. Rev. B Condens. Matter Mater. Phys.* **88**, 205427 (2013).
61. Autore, M. et al. Terahertz plasmonic excitations in Bi_2Se_3 topological insulator. *J. Phys.: Condens. Matter* **29**, 183002 (2017).
62. Analytis, J. G. et al. Two-dimensional surface state in the quantum limit of a topological insulator. *Nat. Phys.* **6**, 960–964 (2010).
63. Brahlek, M., Koirala, N., Salehi, M., Bansal, N. & Oh, S. Emergence of decoupled surface transport channels in bulk insulating Bi_2Se_3 thin films. *Phys. Rev. Lett.* **113**, 026801 (2014).
64. Wang, G. & Cagin, T. Investigation of effective mass of carriers in Bi_2Te_3/Sb_2Te_3 superlattices via electronic structure studies on its component crystals. *Appl. Phys. Lett.* **89**, 152101 (2006).
65. Kim, Y. S. et al. Thickness-dependent bulk properties and weak antilocalization effect in topological insulator Bi_2Se_3 . *Phys. Rev. B Condens. Matter Mater. Phys.* **84**, 073109 (2011).
66. Shikin, A. M. et al. Electronic and spin structure of the topological insulator $Bi_2Te_{2.4}Se_{0.6}$. *Phys. Rev. B Condens. Matter Mater. Phys.* **89**, 125416 (2014).
67. Ginley, T. P. & Law, S. Coupled Dirac plasmons in topological insulators. *Adv. Opt. Mater.* **6**, 1800113 (2018).
68. Wunsch, B., Stauber, T., Sols, F. & Guinea, F. Dynamical polarization of graphene at finite doping. *N. J. Phys.* **8**, 318 (2006).
69. Brahlek, M., Kim, Y. S., Bansal, N., Edrey, E. & Oh, S. Surface versus bulk state in topological insulator Bi_2Se_3 under environmental disorder. *Appl. Phys. Lett.* **99**, 012109 (2011).
70. Li, P. et al. Hyperbolic phonon-polaritons in boron nitride for near-field optical imaging and focusing. *Nat. Commun.* **6**, 7507 (2015).
71. Dai, S. et al. Subdiffractive focusing and guiding of polaritonic rays in a natural hyperbolic material. *Nat. Commun.* **6**, 6963 (2015).
72. Schuller, J. A. et al. Plasmonics for extreme light concentration and manipulation. *Nat. Mater.* **9**, 193–204 (2010).
73. Caldwell, J. D. et al. Atomic-scale photonic hybrids for mid-infrared and terahertz nanophotonics. *Nat. Nanotechnol.* **11**, 9–15 (2016).
74. Xia, F., Wang, H., Xiao, D., Dubey, M. & Ramasubramanian, A. Two-dimensional material nanophotonics. *Nat. Photonics* **8**, 899–907 (2014).
75. Liu, X. & Hersam, M. C. 2D materials for quantum information science. *Nat. Rev. Mater.* **4**, 669–684 (2019).
76. Tang, W. et al. Ultrasensitive room-temperature terahertz direct detection based on a bismuth selenide topological insulator. *Adv. Funct. Mater.* **28**, 1801786 (2018).

Acknowledgements

This work was supported by the European Research Council through the ERC Consolidator Grant (681379) SPRINT from the European Union through Eu Horizon 2020 research and innovation programme Graphene Flagship (GrapheneCore3), the H2020-MSCA-ITN-2017 TeraApps (765426) M.S.V. acknowledges partial support from the second half of the Balzan Prize 2016 in applied photonics delivered to Federico Capasso. The authors thank Prof. Jih-Sheng Wu for sharing suggestions and insights for modeling the near-field response of Bi_2Te_3 .

Author contributions

M.S.V. conceived the experiment. E.A.A.P. set up the experiment and acquired the experimental data. E.A.A.P. simulated the mode dispersion and the near-field response. L.V. fabricated, characterized the samples, and contributed to interpret the data; A.P. grew the TI crystals and characterized their physicochemical properties; G.S. and M.B. performed the simulations of the bulk response in the near-field. The manuscript was written and the data interpreted by E.A.A.P. and M.S.V. All authors contributed to the discussion and to the final manuscript. All work was coordinated and supervised by M.S.V.

Competing interests

The authors declare no competing interests.

Additional information

Supplementary information The online version contains supplementary material available at <https://doi.org/10.1038/s41467-021-26831-6>.

Correspondence and requests for materials should be addressed to Eva Arianna Aurelia Pogna or Miriam Serena Vitiello.

Peer review information *Nature Communications* thanks the anonymous reviewer(s) for their contribution to the peer review of this work.

Reprints and permission information is available at <http://www.nature.com/reprints>

Publisher's note Springer Nature remains neutral with regard to jurisdictional claims in published maps and institutional affiliations.



Open Access This article is licensed under a Creative Commons Attribution 4.0 International License, which permits use, sharing, adaptation, distribution and reproduction in any medium or format, as long as you give appropriate credit to the original author(s) and the source, provide a link to the Creative Commons license, and indicate if changes were made. The images or other third party material in this article are included in the article's Creative Commons license, unless indicated otherwise in a credit line to the material. If material is not included in the article's Creative Commons license and your intended use is not permitted by statutory regulation or exceeds the permitted use, you will need to obtain permission directly from the copyright holder. To view a copy of this license, visit <http://creativecommons.org/licenses/by/4.0/>.

© The Author(s) 2021, corrected publication 2021